

# Anisotropic polarization-induced conductance at a ferroelectric–insulator interface

Yi Zhang<sup>1</sup>, Haidong Lu<sup>2</sup>, Lin Xie<sup>3</sup>, Xingxu Yan<sup>1</sup>, Tula R. Paudel<sup>2</sup>, Jeongwoo Kim<sup>4</sup>, Xiaoxing Cheng<sup>5</sup>, Hui Wang<sup>4</sup>, Colin Heikes<sup>6</sup>, Linze Li<sup>1</sup>, Mingjie Xu<sup>1</sup>, Darrell G. Schlom<sup>6,7</sup>, Long-Qing Chen<sup>5</sup>, Ruqian Wu<sup>4</sup>, Evgeny Y. Tsybmal<sup>2</sup>, Alexei Gruverman<sup>1,2\*</sup> and Xiaoqing Pan<sup>1,4\*</sup>

**Coupling between different degrees of freedom, that is, charge, spin, orbital and lattice, is responsible for emergent phenomena in complex oxide heterostructures<sup>1,2</sup>. One example is the formation of a two-dimensional electron gas (2DEG) at the polar/non-polar LaAlO<sub>3</sub>/SrTiO<sub>3</sub> (LAO/STO)<sup>3–7</sup> interface. This is caused by the polar discontinuity and counteracts the electrostatic potential build-up across the LAO film<sup>3</sup>. The ferroelectric polarization at a ferroelectric/insulator interface can also give rise to a polar discontinuity<sup>8–10</sup>. Depending on the polarization orientation, either electrons or holes are transferred to the interface, to form either a 2DEG or two-dimensional hole gas (2DHG)<sup>11–13</sup>. While recent first-principles modelling predicts the formation of 2DEGs at the ferroelectric/insulator interfaces<sup>9,10,12–14</sup>, experimental evidence of a ferroelectrically induced interfacial 2DEG remains elusive. Here, we report the emergence of strongly anisotropic polarization-induced conductivity at a ferroelectric/insulator interface, which shows a strong dependence on the polarization orientation. By probing the local conductance and ferroelectric polarization over a cross-section of a BiFeO<sub>3</sub>-TbScO<sub>3</sub> (BFO/TSO) (001) heterostructure, we demonstrate that this interface is conducting along the 109° domain stripes in BFO, whereas it is insulating in the direction perpendicular to these domain stripes. Electron energy-loss spectroscopy and theoretical modelling suggest that the anisotropy of the interfacial conduction is caused by an alternating polarization associated with the ferroelectric domains, producing either electron or hole doping of the BFO/TSO interface.**

We explored 400-nm-thick (001)<sub>p</sub>-oriented BFO thin films grown on insulating (110)<sub>o</sub> TSO single-crystalline substrates by molecular beam epitaxy with [100]<sub>p</sub> BFO//[110]<sub>o</sub> TSO and [010]<sub>p</sub> BFO//[001]<sub>o</sub> TSO (where the subscripts p and o represent pseudocubic and orthorhombic indices, respectively, and // means parallel). Details of the film growth are given in the Methods. As schematically shown in Fig. 1a, the BFO thin films exhibit typical striped domain patterns with the 109° domain walls aligned in the [110]<sub>o</sub> direction of the TSO substrate. The out-of-plane polarization component points either downward (towards the substrate) or upward (away from the substrate) across the domain array, leading to a periodic distribution of positive and negative bound charges at the interface. The 109° striped domain structure is

observed by piezoresponse force microscopy (PFM) (Fig. 1b) and by transmission electron microscopy (TEM) (Fig. 1c,d). Figure 1c displays a TEM bright-field image of the cross-section of the BFO/TSO heterostructure, showing the single-crystalline film with few defects and ordered 109° domain arrays. Figure 1d shows an atomic-resolution scanning transmission electron microscopy (STEM) high-angle annular dark-field (HAADF) image of the interface, and the corresponding polarization mapping is presented in the Supplementary Fig. 1. The atomic-scale X-ray energy-dispersive spectroscopy (EDS) mapping and HAADF image intensity profiles across the BFO/TSO interface reveal that the BFO/TSO interface is atomically sharp (Supplementary Figs. 2 and 3).

To investigate the electrical properties of the BFO/TSO interface, we developed a multimodal approach based on probing the cross-sectional specimens of the same sample by a combination of TEM, PFM and conductive atomic force microscopy (CAFM). Details of the sample preparation and geometry of the PFM measurements are given in the Methods and illustrated in Supplementary Fig. 4. To observe the domain structures, the specimens were prepared by cutting along the (110)<sub>o</sub> and (001)<sub>o</sub> planes of the TSO substrate (perpendicular and parallel to the domain stripes in the BFO film, respectively). A PFM image of the 109° domain structure on a cross-sectional specimen is shown in Fig. 2a, which is consistent with the TEM results in Fig. 1c,d. The lower-magnification PFM images of the cross-sectional specimens show a uniform domain structure in the BFO sample (Supplementary Fig. 5).

Figure 2b shows a CAFM map of the same region as in Fig. 2a. The CAFM contrast here represents conductivity along the [110]<sub>o</sub> direction of the TSO substrate (which is parallel to the 109° domain stripes in the BFO film). A current signal can be clearly seen at the BFO/TSO interface. Closer inspection of the CAFM map in Fig. 2b shows that the spatial distribution of the current varies with the change in the polarization direction. By correlating the PFM and CAFM maps, we find that the conducting channel is broader when the polarization is pointing towards the interface (downward polarization state), while it becomes narrower when the polarization is pointing away from the interface (upward polarization state). The averaged current profile in Fig. 2c shows that the interface current is stronger for the downward polarized domains, which is further corroborated by the current–voltage (*I*–*V*) spectroscopic measurements at the interface regions with upward and downward

<sup>1</sup>Department of Materials Science and Engineering, University of California, Irvine, CA, USA. <sup>2</sup>Department of Physics and Astronomy & Nebraska Center for Materials and Nanoscience, University of Nebraska, Lincoln, NE, USA. <sup>3</sup>National Laboratory of Solid State Microstructures and College of Engineering and Applied Sciences, Nanjing University, Nanjing, Jiangsu, China. <sup>4</sup>Department of Physics and Astronomy, University of California, Irvine, CA, USA. <sup>5</sup>Department of Materials Science and Engineering, Penn State University, University Park, PA, USA. <sup>6</sup>Department of Materials Science and Engineering, Cornell University, Ithaca, NY, USA. <sup>7</sup>Kavli Institute at Cornell for Nanoscale Science, Ithaca, NY, USA. \*e-mail: [agruverman2@unl.edu](mailto:agruverman2@unl.edu); [xiaoqing.pan@uci.edu](mailto:xiaoqing.pan@uci.edu)

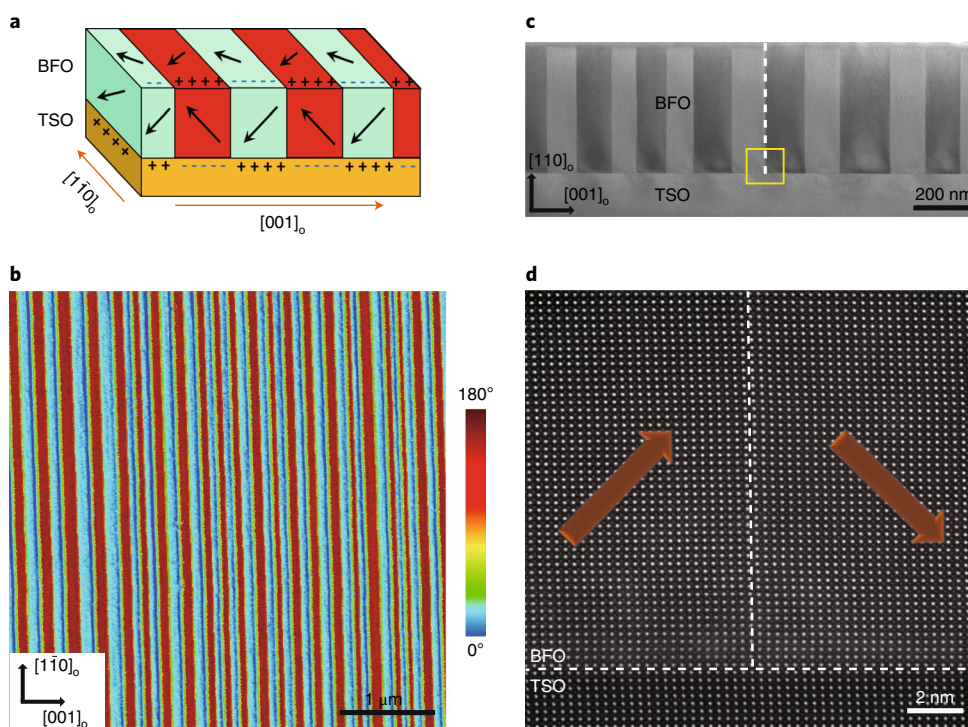


**Fig. 1 | Domain structure in BFO films with 109° domain arrays.** **a**, Schematic of the BFO/TSO heterostructure with 109° domain arrays. The black arrows indicate the polarization direction. '+' and '-' indicate positive and negative bound charges, which are produced by the alternating out-of-plane polarization vectors. **b**, PFM phase image of the BFO sample with 109° domain structure. **c**, Low-magnification TEM image of a cross-section of the BFO/TSO heterostructure. **d**, High-resolution HAADF-STEM image of the 109° domain wall corresponding to the area marked by the yellow box in **c**. Orange arrows indicate polarization direction, and dashed lines indicate the position of the 109° domain wall and the BFO/TSO interface.

polarizations (Fig. 2f). To gain better statistics, we performed histogram analysis of the interface conductivity for upward and downward polarization states (Fig. 2g). The current signal distribution shows that the interface with downward polarization on average exhibits a current signal that is approximately 50% higher than an interface with upward polarization.

Surprisingly, the interface conductivity along the  $[001]_o$  direction of the TSO substrate (which is perpendicular to the 109° domain stripes in the BFO film) reveals a drastically different behaviour. Figure 2d shows a uniform contrast in the PFM image of this surface of the cross-sectional sample, which indicates its monodomain state due to the fact that the 109° domain walls are underneath the surface of the cross-sectional sample and run parallel to it. Figure 2e displays the CAFM image for the same region. No interfacial conductance is observed, indicating the insulating behaviour of the BFO/TSO interface in the direction perpendicular to the 109° stripe domains. Comparison of the current profiles and the  $I$ - $V$  curves measured along the two orthogonal  $[001]_o$  and  $[1\bar{1}0]_o$  directions further confirms strong anisotropy of the interface conductivity (Fig. 2h and the inset).

To understand the origin of the observed conductivity and its anisotropy at the ferroelectric/insulator interface, first-principles calculations were performed. Figure 3 shows the atomic structure of the BFO/TSO(001) superlattice that was used in our calculations (see details in the Methods). Two polarization states, pointing either towards the interface (interface 1) or away from the interface (interface 2, as a result of the periodic boundary conditions used in the calculations), were modelled (Fig. 3a). The resulting layer-resolved density of states (DOS) in Fig. 3a reveals that the ferroelectric polarization produces a rigid shift of the DOS, resulting in the accumulation of electrons at interface 1 and holes at interface 2.

These accumulated free carriers form either an n-type or p-type conducting interface, depending on polarization orientation. Note that in this calculation a critical thickness of BFO, which is 10 unit cells (u.c.) according to the modelling results, is required for the Fermi level to touch the valence band or conduction band. Supplementary Fig. 6 shows the calculated layer-resolved DOS for BFO layer thickness of 8 u.c. This thickness is less than the critical thickness of BFO and hence there is no charge accumulation at the interface, as is evident from the Fermi energy (vertical solid line in Supplementary Fig. 6) lying in the energy gap of the heterostructure. Experimentally we tested a 2 nm (5 u.c.) BFO film on the same cross-sectional surface as in Fig. 2. We did not observe any interfacial conductivity at the BFO/TSO interface (Supplementary Fig. 7).

Comparing these theoretical results to our experimental data, we argue that the conductivity at the BFO/TSO interface is induced by the formation of the alternating n- and p-doped regions associated with the polarization of ferroelectric domains pointing to the interface or away from it, respectively. The measured conductivity depends on the cut of the sample: high conductivity is measured along the stripe domain walls (Fig. 2a,b) and low conductivity in the direction perpendicular to them (Fig. 2d,e). In comparison with the p-type regions, the n-type regions are expected to have higher conductivity due to the higher mobility of electrons. For this reason, we observe the interfacial conductivity modulated by the periodical 109° stripe domain structure (Fig. 2b,g). The conducting path along this direction encounters the periodically repeating p-n and n-p junctions formed at the 109° domain walls so that the electric current in the  $[001]_o$  direction is blocked by these junctions. This also explains the observed insulating behaviour of the interface in the  $[001]_o$  direction, that is, perpendicular to the 109° domain stripes.

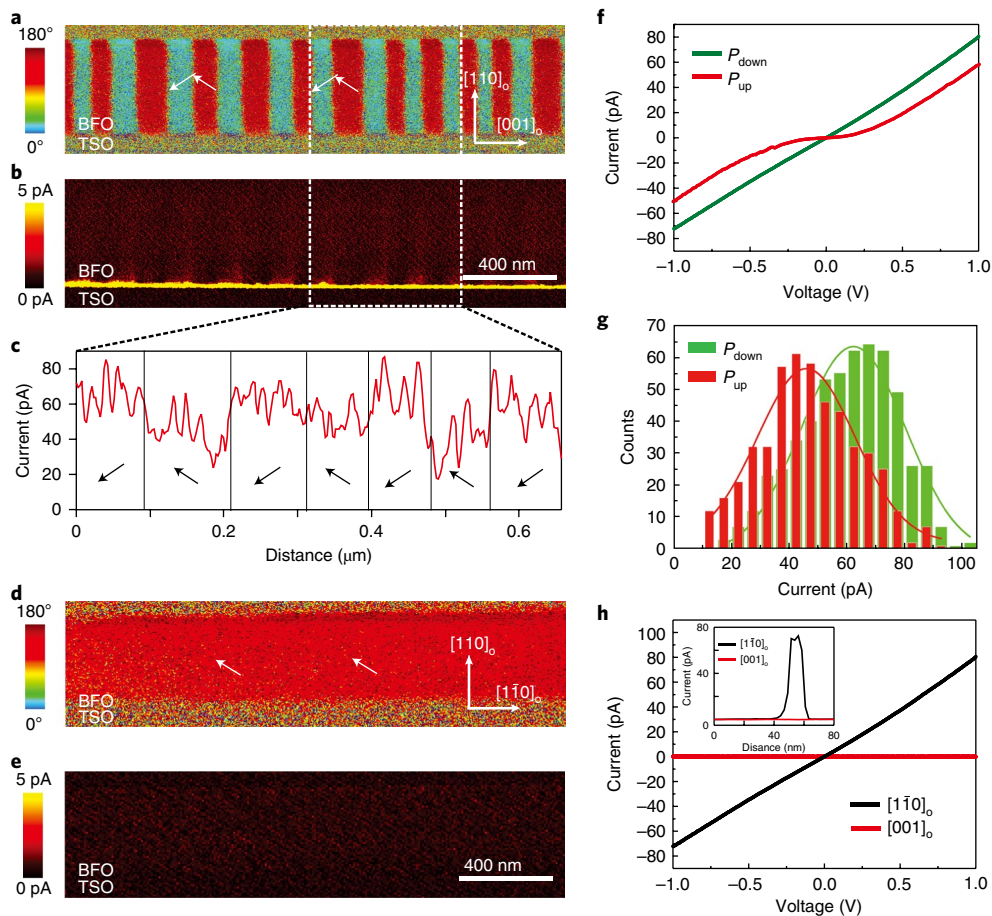


**Fig. 2 | Anisotropic interfacial conduction at the BFO/TSO interface with  $109^\circ$  domain arrays.** **a**, PFM image of the cross-section of a BFO film, cut perpendicular to the stripe domain. The white arrows indicate the three-dimensional polarization vector. **b**, CAFM image of the same region as in **a**. **c**, An averaged current signal profile along the BFO/TSO interface, corresponding to the segment marked by the white dashed lines in **b**. **d**, PFM image of the cross-section of a BFO film, cut parallel to the domain stripe. The white arrows indicate the 3-dimensional polarization vector. **e**, CAFM image of the same region as in **d**. **f**,  $I$ - $V$  curves measured at the BFO/TSO interface regions with different polarization directions ( $P_{\text{down}}$ , polarization pointing towards the BFO/TSO interface;  $P_{\text{up}}$ , polarization pointing away from the BFO/TSO interface). **g**, Histogram of the current for different polarization directions in **b**. **h**,  $I$ - $V$  curves measured at the BFO/TSO interfaces in the samples cut perpendicular and parallel to the stripe domain walls. The inset shows the current profiles across the BFO/TSO interface, which were extracted from **b** and **e**.

These results are corroborated by the phase-field simulations. Figure 3b and c shows a schematic of the  $109^\circ$  domain structure and an alternating bound charge at the interface driven by the periodic change in polarization direction, and Fig. 3d shows the corresponding calculated potential profile at the BFO/TSO interface perpendicular to the  $109^\circ$  domain walls. The alternating positive and negative bound charges at the interface builds a recurring potential barrier for free carriers, making the interface insulating in the direction perpendicular to the domain stripes, at the same time activating electron- or hole-type conduction in the direction parallel to the domain stripes.

The proposed model is further confirmed by atomic-resolution electron energy-loss spectroscopy (EELS) (see Methods for details). Spatial-dependent EELS of O K and Fe  $L_{2,3}$  edges is acquired from regions with two different polarization states as a function of a distance from the BFO/TSO interface (Fig. 4a). Owing to a linear relationship between the onset energy in EELS and the oxidation state of Fe (refs <sup>15,16</sup>), the energy onset difference between O K and Fe  $L_3$  edges reflects the local chemical shift of the Fe oxidation state. We find that this energy onset difference at interface2 is higher over the first four unit cells of BFO than that in the bulk phase, indicating

a higher valence state of Fe (Fig. 4b). In comparison, the energy onset difference in BFO near interface1 is lower than that in the bulk phase, showing a reduced valence state of Fe (Fig. 4b). These results indicate that interface2 with a higher oxidation state of Fe shows a hole-doped p-type conductivity, whereas interface1 with a reduced valence state of Fe exhibits electron-doped n-type conductivity. These conducting channels are confined within an  $\sim 1.5$ -nm-wide region of BFO near the BFO/TSO interface. Estimation of the carrier concentration at the two interfaces based on the EELS data<sup>16</sup> (Fig. 4b) yields  $(0.14 \pm 0.06)$  electrons per unit cell for interface1 and  $(0.15 \pm 0.08)$  holes per unit cell for interface2. Hence, the n- and p-carrier concentration at the two types of the BFO/TSO interface are on the order of  $10^{13} \text{ cm}^{-2}$ . Therefore, we assume that the conductivity difference between interface1 and interface2 is determined by the carrier mobility. Moreover, the energy onset difference of the Fe-O edges across the  $109^\circ$  domain wall shows a step-like transition (Supplementary Fig. 8), which corroborates different Fe valence states and a transition from electron- to hole-doping at the domain wall. Therefore, this step-like distribution of onset energy provides strong evidence of the p-n junction scenario across the  $109^\circ$  domain wall.

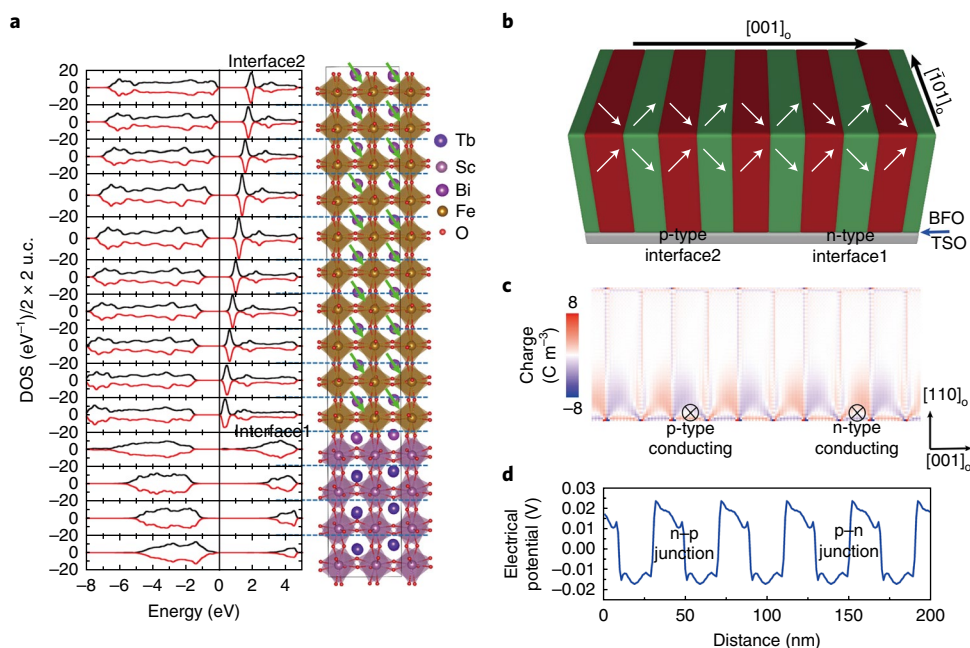


**Fig. 3 | Mechanism for the anisotropic interfacial conduction.** **a**, Layer-resolved DOS for BFO/TSO (001) interfaces obtained from first-principles calculations. Ferroelectric polarization produces a rigid shift of the DOS of BFO, resulting in accumulation of electrons at interface 1 (polarization pointing towards the interface) and holes at interface 2 (polarization pointing away from the interface). The periodic boundary conditions are used in the calculations so that the TSO layers continue to be on top of interface 2. The green arrows indicate the polarization directions. **b–d**, Results of the phase-field simulations. **b**, Domain structure of BFO with  $109^\circ$  domain walls. The white arrows indicate the polarization directions. **c**, Bound charge distribution at the BFO/TSO interface along the domain stripes. **d**, Potential profile at the BFO/TSO interface perpendicular to the domain stripes.

The width of the conducting channel is determined by the screening length of the polarization charge in BFO. Within the Thomas-Fermi approximation, the screening length  $\delta$  can be estimated as<sup>17</sup>

$$\delta = \frac{1}{e} \sqrt{\frac{\epsilon}{\rho_F}} \quad (1)$$

where  $\epsilon$  is the background dielectric permittivity of BFO,  $e$  is the elementary charge and  $\rho_F$  is the DOS at the Fermi energy. Assuming that the dielectric permittivity of BFO is  $\sim 100\epsilon_0$  (refs<sup>18–20</sup>) and  $\rho_F \sim 1 \text{ eV}^{-1}$  per u.c. (Fig. 3a), we obtain  $\delta \sim 1 \text{ nm}$ , which is in agreement with the measured 1.5-nm thickness of the conducting channel. Moreover, we find that the  $109^\circ$  domain arrays are switchable by applying a voltage to the film surface (Supplementary Fig. 9). Hence, the conducting BFO/TSO interface can facilitate ferroelectric switching and could enable the interface conductivity to be controlled via polarization reversal.

In principle, oxygen vacancy redistribution may also contribute to the BFO/TSO interface conductivity<sup>21</sup>. However, although oxygen vacancies in BFO may lead to electron doping and n-type conduction, this mechanism does not explain the anisotropic conductance. Detailed analysis of EELS line scans of the O K edge across the BFO/TSO interfaces (Supplementary Fig. 10 and Supplementary Note 1) shows that the polarization direction in BFO does not affect the oxygen stoichiometry near the interface. Consequently, the oxygen-vacancy-related mechanism of interface conductivity can be ruled out. The Schottky barrier variations at the BFO/Au interface at the back of the cross-sectional sample may also be a potential mechanism behind the observed polarization-related changes in the BFO/TSO interface conductivity. We argue that the change in conductivity due to the different values of the Schottky barrier at the BFO/Au interface for different in-plane components of polarization (pointing towards or away from the BFO/Au interface) associated with the stripe domains is not expected to be as large as that observed

experimentally (see detailed analysis in Supplementary Note 2). This conclusion was proved experimentally by testing a 200-nm-thick BFO film with periodical  $71^\circ$  domain walls (see Supplementary Fig. 11 and Supplementary Note 3 for details).

In conclusion, using a combination of different local probe techniques, we have directly observed polarization-dependent interfacial anisotropic conductivity at the ferroelectric/insulator BFO/TSO interfaces. We found that the orientation of ferroelectric domain walls dramatically changes the interface conductivity: the interface is conducting in the direction parallel to the domain stripes but is insulating in the direction perpendicular to them. Theoretical modelling suggests that the ferroelectric  $109^\circ$  striped domain structure gives rise to alternating n- and p-type conducting channels resulting in polarization-induced interfacial conductivity in the direction parallel to the stripe domains. The formation of p–n junctions at the domain walls blocks the conducting path and makes the interface insulating perpendicular to the stripe domains. Atomic-resolution EELS analysis of the BFO/TSO interface reveals the higher oxidation state of Fe at the p-type conducting interface, while a reduced valence state of Fe is observed at the n-type conducting interface. Our results open exciting possibilities to engineer novel nanoelectronics systems, where control of the ferroelectric polarization allows modulation of the two-dimensional anisotropic electronic transport, providing a new route for advanced device applications.

#### Online content

Any methods, additional references, Nature Research reporting summaries, source data, statements of data availability and associated accession codes are available at <https://doi.org/10.1038/s41565-018-0259-z>.

Received: 30 October 2017; Accepted: 16 August 2018;  
Published online: 24 September 2018

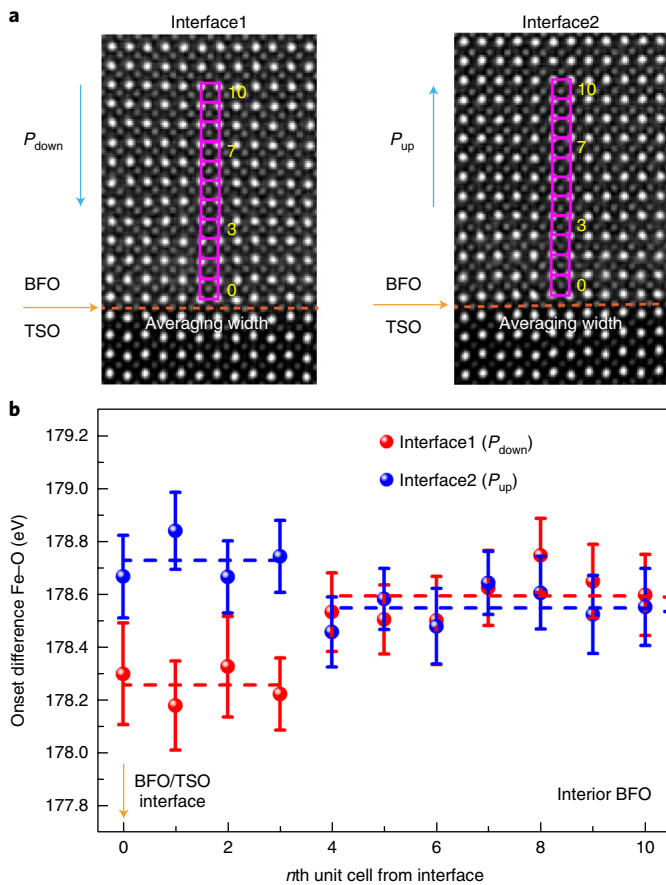


**Fig. 4 | STEM and EELS measurements at the BFO/TSO interface.**

**a**, HAADF-STEM images obtained at the BFO/TSO interface with down and up polarizations. Separate high-resolution linescans were taken at each interface. An EELS linescan averaged within a larger area was carried out at the BFO/TSO interface. Horizontal lines indicate the direction of averaging parallel to the interface. Position 0 is the interfacial unit cell in BFO. The orange arrows indicate the BFO/TSO interface. The blue arrows indicate the polarization direction. **b**, The energy onset difference between the O K and Fe  $L_3$  edges obtained from the BFO/TSO interface to interior BFO via EELS linescans: interface 1 with the polarization pointing towards the BFO/TSO interface ( $P_{down}$ ), red dots; interface 2 with polarization pointing away from the BFO/TSO interface ( $P_{up}$ ), blue dots. The error bars represent the standard error in the peak fitting process for determining the onset energy of the O K and Fe  $L_3$  edges. The red and blue dashed lines are the averaged values of the energy onset difference between the O K and Fe  $L_3$  edges in interface 1 and interface 2, respectively.

## References

- Hwang, H. Y. et al. Emergent phenomena at oxide interfaces. *Nat. Mater.* **11**, 103–113 (2012).
- Sulpizio, J. A., Ilani, S., Irvin, P. & Levy, J. Nanoscale phenomena in oxide heterostructures. *Annu. Rev. Mater. Res.* **44**, 117–149 (2014).
- Ohtomo, A. & Hwang, H. Y. A high-mobility electron gas at the  $\text{LaAlO}_3/\text{SrTiO}_3$  heterointerface. *Nature* **427**, 423–426 (2004).
- Reyren, N. et al. Superconducting interfaces between insulating oxides. *Science* **317**, 1196–1199 (2007).
- Brinkman, A. et al. Magnetic effects at the interface between non-magnetic oxides. *Nat. Mater.* **6**, 493–496 (2007).
- Bert, J. A. et al. Direct imaging of the coexistence of ferromagnetism and superconductivity at the  $\text{LaAlO}_3/\text{SrTiO}_3$  interface. *Nat. Phys.* **7**, 767–771 (2011).
- Salluzzo, M. et al. Origin of interface magnetism in  $\text{BiMnO}_3/\text{SrTiO}_3$  and  $\text{LaAlO}_3/\text{SrTiO}_3$  heterostructures. *Phys. Rev. Lett.* **111**, 087204 (2013).

- Chen, Y. Z. et al. Creation of high mobility two-dimensional electron gases via strain induced polarization at an otherwise nonpolar complex oxide interface. *Nano Lett.* **15**, 1849–1854 (2015).
- Niranjan, M. K., Wang, Y., Jaswal, S. S. & Tsymbal, E. Y. Prediction of a switchable two-dimensional electron gas at ferroelectric oxide interfaces. *Phys. Rev. Lett.* **103**, 016804 (2009).
- Yin, B., Puente, P. A., Qu, S. & Artacho, E. Two-dimensional electron gas at the  $\text{PbTiO}_3/\text{SrTiO}_3$  interface: an ab initio study. *Phys. Rev. B* **92**, 115406 (2015).
- Marshall, S. J. et al. Conduction at a ferroelectric interface. *Phys. Rev. Appl.* **2**, 051001 (2014).
- Fredrickson, K. D. & Demkov, A. A. Switchable conductivity at the ferroelectric interface: nonpolar oxides. *Phys. Rev. B* **91**, 115126 (2015).
- Puente, P. A. et al. Model of two-dimensional electron gas formation at ferroelectric interfaces. *Phys. Rev. B* **92**, 035438 (2015).
- Zhang, Z., Wu, P., Chen, L. & Wang, J. L. First-principles prediction of a two dimensional electron gas at the  $\text{BiFeO}_3/\text{SrTiO}_3$  interface. *Appl. Phys. Lett.* **99**, 062902 (2011).
- Tan, H. Y., Verbeeck, J., Abakumov, A. & Tendeloo, G. V. Oxidation state and chemical shift investigation in transition metal oxides by EELS. *Ultramicroscopy* **116**, 24–33 (2012).
- Rojac, T. et al. Domain-wall conduction in ferroelectric  $\text{BiFeO}_3$  controlled by accumulation of charged defects. *Nat. Mater.* **16**, 322–327 (2017).
- Yong, W. et al. Ferroelectric instability under screened Coulomb interactions. *Phys. Rev. Lett.* **109**, 247601 (2012).
- Nelson, C. T. et al. Domain dynamics during ferroelectric switching. *Science* **334**, 968–971 (2011).
- Ihlefeld, J. F. et al. Effect of domain structure on dielectric nonlinearity in epitaxial films. *Appl. Phys. Lett.* **97**, 262904 (2010).
- Lim, S. H. et al. Enhanced dielectric properties in single crystal-like thin films grown by flux-mediated epitaxy. *Appl. Phys. Lett.* **92**, 012918 (2008).
- Cen, C. et al. Nanoscale control of an interfacial metal–insulator transition at room temperature. *Nat. Mater.* **7**, 298–302 (2008).

## Acknowledgements

The work was supported by the Department of Energy (DOE), Office of Basic Energy Sciences, Division of Materials Sciences and Engineering under award DE-SC0014430 and partially by the National Science Foundation (NSF) under grants DMR-1506535 and DMR-1629270. L.X. was supported by the National Basic Research Program of China (grant no. 2015CB654901) and National Natural Science Foundation of China (grant no. 51302132). The research at the University of Nebraska-Lincoln was supported by the NSF through the Nebraska Materials Science and Engineering Center (MRSEC) under grant DMR-1420645. J.K., H.W. and R.Q.W. acknowledge support of DOE-BES (grant no. DE-272 FG02-05ER46237) and computing allocation by NERSC. The work at Penn State is supported by the US Department of Energy under award DE-FG02-07ER46417. The work at Cornell University was supported by the NSF (Nanosystems Engineering Research Center for Translational Applications of Nanoscale Multiferroic Systems) under grant EEC-1160504 (C.H. and D.G.S.). Substrate preparation was performed in part at the Cornell Nanoscale Facility, a member of the National Nanotechnology Coordinated Infrastructure (NNCI), which is supported by the NSF (grant ECCS-1542081). The authors would also like to acknowledge the University of California, Irvine's Materials Research Institute (IMRI) for the use of TEM facilities. Y.Z. would like to thank J. R. Jokisaari for his initial work and help on the PFM measurements carried out at the University of Michigan. The authors also thank T. Aoki (University of California, Irvine) for his help on EELS measurements.

## Author contributions

X.Q.P. and Y.Z. conceived this project and designed experiments. Y.Z. and H.D.L. carried out the scanning probe microscopy experiments and data analysis supervised by A.G. and X.Q.P. X.X.Y., Y.Z. and L.X. carried out the TEM and EELS studies supervised by X.Q.P. T.R.P., J.W.K. and H.W. performed the first-principles modelling supervised by E.Y.T. and R.Q.W. X.X.C. carried out the phase-field simulations supervised by L.-Q.C. Thin films were grown by C.H. supervised by D.G.S. L.Z.L. and M.J.X. participated in the analysis of experimental data. Y.Z., H.D.L., X.Q.P., A.G. and E.Y.T. wrote the manuscript. All authors discussed the results and commented on the manuscript.

## Competing interests

The authors declare no competing interests.

## Additional information

**Supplementary information** is available for this paper at <https://doi.org/10.1038/s41565-018-0259-z>.

**Reprints and permissions information** is available at [www.nature.com/reprints](http://www.nature.com/reprints).

**Correspondence and requests for materials** should be addressed to A.G. or X.P.

**Publisher's note:** Springer Nature remains neutral with regard to jurisdictional claims in published maps and institutional affiliations.

## Methods

**Sample preparation.** The BFO film was grown using a novel kinetically limited absorption-controlled method of reactive molecular beam epitaxy (MBE). Further details of the development and characterization of this method will be given elsewhere (J. Mundy et al., manuscript in preparation). In short, a single-crystal (110)<sub>r</sub> TSO substrate is heated to 650 °C in distilled ozone (~80% ozone) at partial pressure  $4 \times 10^{-6}$  torr. We use situ reflection high-energy electron diffraction (RHEED) to determine the growth conditions for a smooth and surface-reconstruction-free film. In this case, an Fe flux of  $1.7 \times 10^{13}$  atoms  $\text{cm}^{-2} \text{s}^{-1}$  is supplied concurrently with an excess Bi:Fe ratio of ~8 as determined by a quartz crystal microbalance. The growing film surface is monitored periodically with in situ RHEED, and the sources are shuttered to allow for Fe diffusion if the film appears to roughen. Cross-sectional TEM specimens were prepared by mechanical polishing followed by argon ion milling in a Gatan Precision Ion Polishing System II (PIPS II).

**Structural and electrical characterization.** STEM imaging was performed either in a JEOL JEM-3100R05 or in a JEOL Grand ARM300CF electron microscope, both of which are equipped with a cold field emission gun and double spherical aberration correctors with a spatial resolution of ~0.6 Å when operated at 300 kV. HAADF-STEM images were taken with the convergence angle of the incident electrons at 22 mrad and the collection angle at 83–165 mrad. EDS mapping of the BFO/TSO interface was carried out on an FEI Titan with Chemi-STEM operated at 200 kV.

The atomic-resolution EELS was carried out using an aberration-corrected monochromated NION ultra-STEM 200, which has an energy resolution of 4.2 meV at 30 kV, 6.7 meV at 60 kV, and 9 meV at 100 kV. For EELS analysis in this work, the microscope was operated at 100 kV with convergence semi-angle of 30 mrad and a beam current of ~100 pA. EELS data were acquired with a dispersion of 0.164 eV per channel and with the dwell time of 1 s per pixel. The background in each spectrum was removed by power-law function using Gatan's DigitalMicrograph software. The energy loss where the edge reaches 10% of its maximum intensity is taken as the energy onset value for each O K and Fe L<sub>3</sub> edge in each pixel.

PFM measurements were performed using a commercial Asylum Research MFP-3D system. The PPP-EFM probe from Nanosensors was used in this study. 3D vector PFM imaging was performed by collecting a vertical piezoresponse component and two lateral piezoresponse components. The sample was rotated by 90° to discriminate between orthogonally oriented in-plane polar vector components. CAFM measurements were carried out using the same MFP-3D system with ORCA mode. To perform current mapping on the cross-sectional sample, a thin Au layer was deposited on the backside of the specimen. The conducting AFM tip is able to scan the sample from the electron transparent region to much thicker regions (a few micrometres) along the interface of a cross-sectional sample.

**First-principles calculations.** First-principles calculations were performed using density functional theory (DFT) within the projected augmented wave (PAW) method for the electron-ion potential and the generalized gradient approximation (GGA) for exchange and correlation, as implemented in the Vienna ab initio simulation package (VASP)<sup>22,23</sup>. The exchange and correlation beyond GGA were taken into account by introducing an onsite Coulomb repulsion with Hubbard  $U=2.5$  eV (ref. 24) for Fe-3d orbitals in rotationally invariant formalism<sup>25</sup>, as implemented in VASP. The electronic structure of the interface was calculated by constructing a BFO/TSO (001) superlattice containing 8.5 u.c. of the BFO and 3.5 u.c. of the TSO. The ScO<sub>2</sub>/BiO interfaces were assumed to be symmetric with respect to the central BiO layer, ensuring no electric field other than that originating from the ferroelectricity of BiFeO<sub>3</sub> was present. The calculations were carried out using a kinetic energy cutoff of 340 eV and an  $8 \times 8 \times 1$  k-point mesh for

Brillouin zone integration. We fully relaxed *c*-lattice constant and ionic coordinates with the force convergence limit of 0.02 eV atom<sup>-1</sup>. The in-plane lattice constant was fixed to that of the calculated GGA+*U* lattice constant of the  $2 \times 2$  pseudo-cubic unit cell TSO.

**Phase-field simulation.** Phase-field simulation provides information on polarization evolution by solving the time-dependent Ginzburg–Landau equation:

$$\frac{\partial P_i(\mathbf{r}, t)}{\partial t} = -L \frac{\delta F}{\delta P_i(\mathbf{r}, t)}, \quad (i = 1, 2, 3)$$

where  $P_i$  is the order parameter in the Landau theory, and its physical meaning is the component of polarization in the *i*th direction.  $L$  is the kinetic coefficient,  $\mathbf{r}$  represents the spatial position vector,  $t$  denotes the evolution time step, and  $F$  is the total free energy of the BFO with volume  $V$  that can be expressed by the following formula<sup>26–28</sup>

$$F = \int (f_{\text{Landau}} + f_{\text{elastic}} + f_{\text{electric}} + f_{\text{gradient}}) dV$$

where  $f_{\text{Landau}}$ ,  $f_{\text{elastic}}$ ,  $f_{\text{electric}}$  and  $f_{\text{gradient}}$  are the densities of the bulk free energy, elastic energy, electrostatic energy and gradient energy of the BFO, respectively. Owing to the large domain size in the experiment, being beyond the computation capabilities, we scaled down the system size. The size of the simulation system was  $200 \times 100 \times 45$  grids, with each grid point representing 1 nm in real space. The thickness of the substrate, film and vacuum layers was 10 nm, 30 nm and 5 nm, respectively. For the *x* and *y* directions, a periodic boundary condition was adopted. The initial set-up for the simulation was a series of the 109° domain stripes, each 30 nm in width, along the *y* direction. The elastic boundary condition fixes the displacement of 10 grids into the substrate and is traction-free on top of the film surface. No mismatch strain is assumed between the film and substrate. The electric boundary condition is short circuit both for the top surface of the film and for the bottom interface. In the phase-field simulation, the bound charge distribution was obtained by calculating derivatives of polarizations, and the electric potential distribution was then computed by solving the Poisson equation.

## Data availability

The data that support the plots within this paper and other findings of this study are available from the corresponding authors upon reasonable request.

## References

- Kresse, G. & Joubert, D. From ultrasoft pseudopotentials to the projector augmented-wave method. *Phys. Rev. B* **59**, 1758–1775 (1999).
- Kresse, G. & Furthmüller, J. Efficient iterative schemes for ab initio total-energy calculations using a plane-wave basis set. *Phys. Rev. B* **54**, 11169–11186 (1996).
- Paudel, T. R., Jaswal, S. S. & Tsymbal, E. Y. Intrinsic defects in multiferroic BiFeO<sub>3</sub> and their effect on magnetism. *Phys. Rev. B* **85**, 104409 (2012).
- Dudarev, S. L., Botton, G. A., Savrasov, S. Y., Humphreys, C. J. & Sutton, A. P. Electron-energy-loss spectra and the structural stability of nickel oxide: an LSDA+*U* study. *Phys. Rev. B* **57**, 1505–1509 (1998).
- Chen, L. Q. Phase-field model of phase transitions/domain structures in ferroelectric thin films: a review. *J. Am. Ceram. Soc.* **91**, 1835–1844 (2008).
- Li, Y. L., Hu, S. Y., Liu, Z. K. & Chen, L. Q. Effect of substrate constraint on the stability and evolution of ferroelectric domain structures in thin films. *Acta Mater.* **50**, 395–411 (2002).
- Li, Y. L., Hu, S. Y., Liu, Z. K. & Chen, L. Q. Effect of electrical boundary conditions on ferroelectric domain structures in thin films. *Appl. Phys. Lett.* **81**, 427–429 (2002).